




Zeeman spin splittings with persistent spin textures in antiferromagnetic semiconductorsXinran Liu ¹, Hong Jian Zhao,^{1,2,3,*} Laurent Bellaiche,⁴ and Yanming Ma ^{1,3,5,†}¹Key Laboratory of Material Simulation Methods and Software of Ministry of Education, College of Physics, Jilin University, Changchun 130012, China²Key Laboratory of Physics and Technology for Advanced Batteries (Ministry of Education), College of Physics, Jilin University, Changchun 130012, China³International Center of Future Science, Jilin University, Changchun 130012, China⁴Physics Department and Institute for Nanoscience and Engineering, University of Arkansas, Fayetteville, Arkansas 72701, USA⁵State Key Laboratory of Superhard Materials, College of Physics, Jilin University, Changchun 130012, China (Received 4 October 2022; revised 11 April 2023; accepted 22 August 2023; published 5 September 2023)

Realizing sizable Zeeman spin splittings (ZSSs) with persistent spin textures (PSTs) in semiconductors is promising for the design of high-performance spintronic devices. The ZSSs of this kind have long been known in ferromagnetic semiconductors, while whether antiferromagnetic semiconductors—much more plentiful than ferromagnetic semiconductors—can host an analogous effect remains elusive. Here, we show that such ZSSs can occur in antiferromagnetic semiconductors. By symmetry analysis, we find 12 magnetic point groups that can host ZSSs and PSTs, providing theoretical guidelines for screening the corresponding antiferromagnets. Our first-principles calculations further confirm CaTcO₃ as an antiferromagnetic semiconductor showcasing ZSSs that are sizable (tens of meV), possibly controllable by a magnetic field, and accompanied with PSTs. Our work thus may open a route towards the application of antiferromagnetic semiconductors in spintronics.

DOI: [10.1103/PhysRevB.108.125108](https://doi.org/10.1103/PhysRevB.108.125108)**I. INTRODUCTION**

Rashba, Dresselhaus, and Zeeman spin splittings in semiconductors are crucial for quantum computation and the design of spintronic devices [1–4]. Of particular interest are the Zeeman spin splittings (ZSSs) showcasing the nearly homogeneous distribution of electronic spin magnetization in momentum space [referred to as persistent spin textures (PSTs)]: The PSTs enable the nondissipative spin transport of electrons by suppressing the spin relaxation [2,5–7]. Ferromagnetic semiconductors are ideal materials to host sizable ZSSs (e.g., ≥ 26 meV [8]) belonging to the aforementioned kind [4]. Yet ferromagnetic semiconductors are rare in nature, and most of them showcase magnetic Curie temperatures far below room temperature [9–11], limiting the device applications of such materials. In sharp contrast, antiferromagnetic semiconductors are not only much more plentiful than ferromagnetic semiconductors, but also likely to have Néel temperatures near or above room temperature [9,11,12]. The realization of sizable ZSSs with PSTs in antiferromagnetic semiconductors would thus open new doors in semiconductor spintronics. Recent studies indicate that antiferromagnets can host diverse patterns of spin splittings and spin textures (see, e.g., Refs. [13–31]); sizable ZSSs that are controllable by an electric field can be achieved in antiferromagnetic semiconductors (see, e.g., Refs. [28–31]). Nonetheless, the possibility and underlying mechanisms of realizing sizable ZSSs (in

antiferromagnetic semiconductors) that are magnetically controllable and accompanied with PSTs remain unclear.

In this paper, we identify 12 magnetic point groups (MPGs) that are compatible with ZSSs and PSTs by symmetry analysis. Exemplified by *Pnma* perovskite antiferromagnets, we find that ZSSs and PSTs can be generated via the combination of antiferromagnetic vectors and antiferrodistortive motions, thanks to spin-orbit coupling (SOC); a magnetic field is able to control the ZSSs by modifying the orientation of the antiferromagnetic vectors. We further predict, by first-principles calculations, that (i) perovskite CaTcO₃ is a candidate that presents sizable ZSSs (e.g., tens of meV) and (ii) antiferromagnetic CaTcO₃ showcases PSTs in the vicinity of the Brillouin zone's center.

II. METHODS

The Vienna *ab initio* simulation package (VASP) [32,33] is used to perform the first-principles simulations, employing the local spin density approximation (LSDA) [34] within the framework of the projector augmented wave [35]. We solve the $3s^23p^64s^2$ electrons for Ca, $4s^24p^65s^2$ for Sr, $4s^24p^64d^25s^1$ for Y, $3s^1$ for Na, $4d^65s^1$ for Tc, $3d^74s^1$ for Fe, $3d^94s^1$ for Ni, $2s^22p^5$ for F, and $2s^22p^4$ for O, with a cutoff energy of 550 eV. A *k*-point mesh of $6 \times 4 \times 6$ is used to sample the Brillouin zone of the *Pnma* phase of perovskites [20-atom unitcell, sketched in Fig. 1(a)]. As for the non-perovskite Ca₂Fe₂O₅, we use a *k*-point mesh of $6 \times 2 \times 6$, in accordance with its cell (sketched in Fig. S12 of the Supplemental Material (SM) [36], which contains Refs. [37–39]). Employing the LSDA+*U* approach [40], we select

*physzhaohj@jlu.edu.cn

†mym@jlu.edu.cn

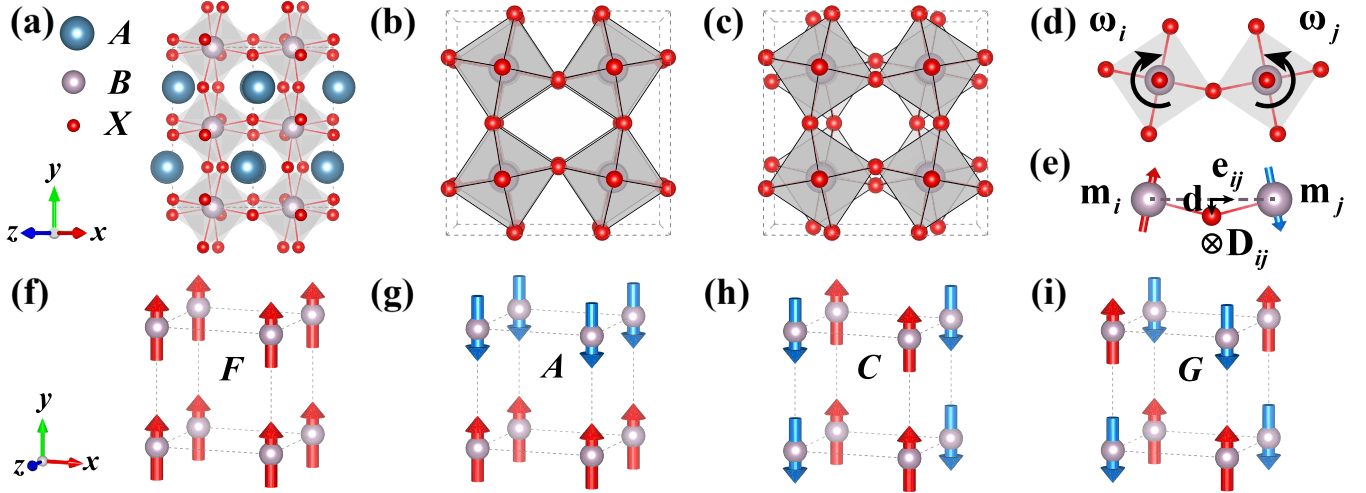


FIG. 1. Schematizations regarding ABX_3 perovskite. (a) Crystal structure of $Pnma$ perovskite. The lattice vectors \mathbf{a} , \mathbf{b} , and \mathbf{c} are along the x , y , and z directions, respectively. (b) In-phase ω_M rotation. (c) Antiphase ω_R rotation. (d) The ω_i and ω_j local rotations (depicted by curled arrows) of two neighboring BX_6 octahedrons centered on i and j sites. (e) The geometry unit yielding the Dzyaloshinskii-Moriya interaction. Here, \mathbf{e}_{ij} is the unit vector along the i - j line, and \mathbf{d} is the displacement vector of the X ion with respect to the i - j line. (f), (g), (h), and (i) F -, A -, C -, and G -type collinear magnetic configurations, respectively, carried by the B sublattice. The cyan and red arrows in (e)–(i) denote the magnetic moments of B ions. The χ (χ being x , y , or z) components of F -, A -, C -, and G -type magnetic vectors are denoted by F_χ , A_χ , C_χ , and G_χ , respectively.

an effective Hubbard U (U_{eff}) of 2 eV for $4d$ orbitals of Tc, and 3 eV for $3d$ orbitals of Fe and Ni, to treat the strong correction effect of d electrons. The choice of effective U values for Tc and Fe follows from Refs. [41,42]. We first optimize the crystal structures [without the inclusion of spin-orbit coupling (SOC)] of CaTcO_3 , SrTcO_3 , YFeO_3 , NaNiF_3 , and $\text{Ca}_2\text{Fe}_2\text{O}_5$ with a force convergence criterion of 0.005 eV/Å. Then, we calculate the band structures for them considering various magnetic structures; these band structures are calculated in the framework of noncollinear magnetism, with full SOC or null SOC [43]. Furthermore, the following tools are employed in this paper: VASPKIT [44,45], MATPLOTLIB [46], VESTA [47], SEEK-PATH [48–50], FINDSYM [51–53], MATHEMATICA [54], and BILBAO CRYSTALLOGRAPHIC SERVER [55–57] (MAGNDATA [58–60], MPOINT [61], and MTENSOR [62]).

III. RESULTS AND DISCUSSION

A. Strategies towards realizing the ZSSs and PSTs in antiferromagnets

To begin with, we emphasize that our purpose is to capture the generic features (regarding spin splittings) of various antiferromagnets, instead of focusing on some individual features of a few specific antiferromagnets. In this regard, the orbital hybridization, albeit important in electronic band structures, is fully neglected in our analysis, since orbital hybridization can be distinct in different materials (i.e., not generic).

To derive our models, we recall that the magnetic crystalline materials are assigned to 122 MPGs. These MPGs can be compatible or incompatible with ferromagnetism. For antiferromagnets with a MPG compatible with ferromagnetism [63], a nonzero weak ferromagnetic component F_β is allowed by symmetry, which can be thought of as the magnetization induced by the effective magnetic field B_α inside the material

($\alpha, \beta = x, y, z$). The component F_β connects with the B_α field via $F_\beta = \chi_{\text{eff}}^{\beta,\alpha} B_\alpha$, where $\chi_{\text{eff}}^{\beta,\alpha}$ is the effective magnetic susceptibility. This implies an energetic coupling $\Lambda_{\alpha,\beta} B_\alpha F_\beta$ with $\Lambda_{\alpha,\beta}$ being the coefficient. As a matter of fact, F_β transforms identically as the electronic spin angular momentum operator \hat{S}_β (represented by the Pauli matrix σ_β) under spatial or temporal symmetry operations; the coupling $\Delta_{\alpha,\beta} B_\alpha \sigma_\beta$ is thus symmetrically allowed as well. The $\Delta_{\alpha,\beta} B_\alpha \sigma_\beta$ coupling indicates ZSSs in antiferromagnetic materials (if any), where $\Delta_{\alpha,\beta} B_\alpha$ characterizes the splitting magnitude. In this sense, the ZSSs in antiferromagnets are driven by the effective magnetic field instead of the weak ferromagnetism [64]. Accordingly, external stimuli (e.g., a magnetic field) may be able to manipulate the ZSSs by controlling the B_α effective field. We will come back to this point in the following sections.

Towards the goal of realizing PSTs, a natural idea is to exclude the MPGs that allow the linear-in- k spin splittings [e.g., $k_\alpha \sigma_\beta$, $k \equiv (k_x, k_y, k_z)$ being the wave vector] [65]. Such an exclusion implies that the electronic spin textures are nearly momentum independent when k is small. Previous symmetry analysis indicates that 18 MPGs (i.e., $11'$, $21'$, $31'$, $41'$, $61'$, $m1'$, $mm21'$, $3m1'$, $4mm1'$, $6mm1'$, $2221'$, $321'$, $4221'$, $6221'$, $\bar{4}1'$, $\bar{4}2m1'$, $231'$, and $4321'$) and their subgroups host the $k_\alpha \sigma_\beta$ -type coupling [66]; these MPGs should be excluded. Following this, we analyze the rest of the MPGs and identify 12 MPGs that (i) are compatible with ferromagnetism and (ii) do not involve the linear-in- k spin splittings. The 12 MPGs and the corresponding H_{eff} (for the description of ZSSs) are shown in Table I. Our derived H_{eff} can also describe the ZSSs (at the Γ point of the Brillouin zone) in crystalline antiferromagnets, given that (i) the antiferromagnet belongs to type I or type III magnetic space groups [67] and (ii) the corresponding MPG of the antiferromagnet is one of the cases listed in Table I.

TABLE I. The MPGs that possibly yield ZSSs, with the $k_\alpha\sigma_\beta$ -type couplings being forbidden by symmetry. For each MPG, the \mathbf{F} and \mathbf{B}_{eff} indicate the symmetrically allowed ferromagnetism and effective magnetic field, respectively; the effective Hamiltonian H_{eff} implies the possible ZSSs arising from the effective magnetic field \mathbf{B}_{eff} .

MPGs	\mathbf{F}	\mathbf{B}_{eff}	H_{eff}
$\bar{1}$	(F_x, F_y, F_z)	$(\mathcal{B}_x, \mathcal{B}_y, \mathcal{B}_z)$	$\Delta_{\alpha,\beta}\mathcal{B}_\alpha\sigma_\beta$ ($\alpha, \beta = x, y, z$)
$2/m$	$(0, F_y, 0)$	$(0, \mathcal{B}_y, 0)$	$\Delta_{y,y}\mathcal{B}_y\sigma_y$
$2'/m^a$	$(F_x, 0, F_z)$	$(\mathcal{B}_x, 0, \mathcal{B}_z)$	$\Delta_{\alpha,\beta}\mathcal{B}_\alpha\sigma_\beta$ ($\alpha, \beta = x, z$)
$m'm'm^b$	$(0, 0, F_z)$	$(0, 0, \mathcal{B}_z)$	$\Delta_{z,z}\mathcal{B}_z\sigma_z$
$m'mm'$	$(0, F_y, 0)$	$(0, \mathcal{B}_y, 0)$	$\Delta_{y,y}\mathcal{B}_y\sigma_y$
$mm'm'$	$(F_x, 0, 0)$	$(\mathcal{B}_x, 0, 0)$	$\Delta_{x,x}\mathcal{B}_x\sigma_x$
$4/m$	$(0, 0, F_z)$	$(0, 0, \mathcal{B}_z)$	$\Delta_{z,z}\mathcal{B}_z\sigma_z$
$4/mm'm'$	$(0, 0, F_z)$	$(0, 0, \mathcal{B}_z)$	$\Delta_{z,z}\mathcal{B}_z\sigma_z$
$\bar{3}$	$(0, 0, F_z)$	$(0, 0, \mathcal{B}_z)$	$\Delta_{z,z}\mathcal{B}_z\sigma_z$
$\bar{3}m'$	$(0, 0, F_z)$	$(0, 0, \mathcal{B}_z)$	$\Delta_{z,z}\mathcal{B}_z\sigma_z$
$\bar{6}$	$(0, 0, F_z)$	$(0, 0, \mathcal{B}_z)$	$\Delta_{z,z}\mathcal{B}_z\sigma_z$
$6/m$	$(0, 0, F_z)$	$(0, 0, \mathcal{B}_z)$	$\Delta_{z,z}\mathcal{B}_z\sigma_z$
$\bar{6}m'2'$	$(0, 0, F_z)$	$(0, 0, \mathcal{B}_z)$	$\Delta_{z,z}\mathcal{B}_z\sigma_z$
$6/mm'm'$	$(0, 0, F_z)$	$(0, 0, \mathcal{B}_z)$	$\Delta_{z,z}\mathcal{B}_z\sigma_z$

^aIn $2/m$ and $2'/m'$, the twofold rotation is along the y axis.

^b $m'm'm$, $m'mm'$, and $mm'm'$ belong to the same MPG.

B. Perovskite antiferromagnets: Origin of ZSSs

Table I indicates that $\mathbf{B}_{\text{eff}} \equiv (\mathcal{B}_x, \mathcal{B}_y, \mathcal{B}_z)$ can drive ZSSs in antiferromagnets. In general, the origin of \mathbf{B}_{eff} can be diverse in various antiferromagnets. For example, the occurrence of \mathbf{B}_{eff} does not depend on SOC in electric-field-polarized Fe_2TeO_6 antiferromagnets [28], while it stems from SOC in perovskite antiferromagnets such as rare-earth orthoferrites and orthochromates [68,69]. Here, we take the antiferromagnetic ABX_3 perovskites as our test bed to shed light on one possible origin of \mathbf{B}_{eff} (and ZSSs).

We recall that almost half of the ABX_3 perovskites [70] exhibit GdFeO_3 -type structural distortions [71], yielding the $Pnma$ space group [see Fig. 1(a)]. As sketched in Figs. 1(f)–1(i), the B sublattice typically hosts four collinear magnetic configurations by endowing B ions with magnetism, where F is ferromagnetic and the other three (i.e., A , G , and C) are antiferromagnetic. In $Pnma$ perovskite antiferromagnets [72], the predominant G_y , C_z , C_x , and G_z orderings yield $Pn'm'a$, $Pnm'a'$, $Pn'm'a$, and $Pn'm'a'$ magnetic space groups, resulting in F_z, F_x, F_z , and F_y weak ferromagnetic components, respectively (see, e.g., Refs. [11,73]). These magnetic space groups are associated with the $m'm'm$, $m'mm'$, and $mm'm'$ MPGs listed in Table I, suggesting the symmetrically allowed ZSSs in antiferromagnets.

Structurally, the ABX_3 perovskites have BX_6 octahedrons connected with each other via intermediate X ions. Compared with the high-symmetric cubic phase, the BX_6 octahedrons of $Pnma$ ABX_3 perovskite exhibit two types of primary antiferrodistortive motions [37,38], namely, in-phase ω_M and antiphase ω_R rotations [see Figs. 1(b) and 1(c)]. The ω_R and ω_M antiferrodistortive rotations of $Pnma$ perovskites are along the x and y directions, respectively (see Sec. SI of the SM).

Therefore the B - X - B bond angle is away from 180° , as shown in Fig. 1(d). The non- 180° B - X - B bond angle yields a geometry unit that is responsible for the Dzyaloshinskii-Moriya interaction (DMI) $\mathbf{D}_{ij} \cdot (\mathbf{m}_i \times \mathbf{m}_j)$ [see Fig. 1(e)] [74–76]. The DMI vector $\mathbf{D}_{ij} \propto (\mathbf{d} \times \mathbf{e}_{ij})$ can be further derived as $\mathbf{D}_{ij} = \alpha(\boldsymbol{\omega}_i - \boldsymbol{\omega}_j)$ [68,77,78], where α is a coefficient related to SOC. This establishes the correlation among antiferrodistortive rotation (ω_R or ω_M), SOC, and weak ferromagnetism, noticing that $\mathbf{D}_{ij} \cdot (\mathbf{m}_i \times \mathbf{m}_j)$ can lead to weak ferromagnetism in antiferromagnetic perovskites [68,69]. Previous studies [68,69] indicate the energetic couplings $\delta E = \Lambda'\alpha\omega_{R,x}(G_yF_z - G_zF_y) + \Lambda''\alpha\omega_{M,y}(C_zF_x - C_xF_z)$ describing the weak ferromagnetism in $Pnma$ perovskite antiferromagnets, with Λ' and Λ'' being material-dependent coefficients. Differentiating δE with respect to F_x, F_y , or F_z , the \mathbf{B}_{eff} fields (rooted in $\omega_{R,x}$ or $\omega_{M,y}$) are $\mathbf{B}_{\text{eff}}(\omega_{R,x}) \propto \alpha(-\omega_{R,x}G_y\mathbf{z} + \omega_{R,x}G_z\mathbf{y})$ and $\mathbf{B}_{\text{eff}}(\omega_{M,y}) \propto \alpha(-\omega_{M,y}C_z\mathbf{x} + \omega_{M,y}C_x\mathbf{z})$, where \mathbf{x}, \mathbf{y} , and \mathbf{z} are unit vectors along the x, y , and z directions. Such \mathbf{B}_{eff} fields yield the following effective Hamiltonians:

$$H_{\text{eff}}(\omega_{R,x}) = -\Delta_{R,xyz}\alpha\omega_{R,x}G_y\sigma_z + \Delta_{R,xzy}\alpha\omega_{R,x}G_z\sigma_y,$$

$$H_{\text{eff}}(\omega_{M,y}) = -\Delta_{M,yzx}\alpha\omega_{M,y}C_z\sigma_x + \Delta_{M,yxz}\alpha\omega_{M,y}C_x\sigma_z.$$

Here, the difference between $\Delta_{R,xyz}$ and $\Delta_{R,xzy}$ ($\Delta_{M,yzx}$ and $\Delta_{M,yxz}$) comes from the anisotropy of the $Pnma$ orthorhombic material. The occurrence of α in $H_{\text{eff}}(\omega_{R,x})$ and $H_{\text{eff}}(\omega_{M,y})$ implies the critical role of SOC for ZSSs in perovskite antiferromagnets. According to $H_{\text{eff}}(\omega_{R,x})$, the eigenenergies ($\varepsilon_+, \varepsilon_-$) of G_y and G_z configurations, with the subscript “+” or “−” distinguishing higher and lower sublevels, are $(|\Delta_{R,xyz}\alpha\omega_{R,x}G_y|, -|\Delta_{R,xyz}\alpha\omega_{R,x}G_y|)$ and $(|\Delta_{R,xzy}\alpha\omega_{R,x}G_z|, -|\Delta_{R,xzy}\alpha\omega_{R,x}G_z|)$, respectively. This gives rise to a ZSS of $|2\Delta_{R,xyz}\alpha\omega_{R,x}G_y|$ for the G_y configuration and a ZSS of $|2\Delta_{R,xzy}\alpha\omega_{R,x}G_z|$ for the G_z configuration. The spin magnetization $[S_{\pm,x}, S_{\pm,y}, S_{\pm,z}]$ values associated with the G_y and G_z configurations are given by $[0, 0, \mp\frac{1}{2}\text{sgn}(\Delta_{R,xyz}\alpha\omega_{R,x}G_y)]$ and $[0, \pm\frac{1}{2}\text{sgn}(\Delta_{R,xzy}\alpha\omega_{R,x}G_z), 0]$, respectively [79], where $\text{sgn}(x) = x/|x|$ for $x \neq 0$. Similarly, the ZSS is $|2\Delta_{M,yzx}\alpha\omega_{M,y}C_z|$ for the C_z configuration and $|2\Delta_{M,yxz}\alpha\omega_{M,y}C_x|$ for the C_x configuration. Therefore ZSSs can be realized in $Pnma$ perovskites with (i) G_y or G_z antiferromagnetic configuration, thanks to the $\omega_{R,x}$ rotation, or (ii) C_x or C_z antiferromagnetic configuration, because of the $\omega_{M,y}$ rotation.

Interestingly, the ZSSs in perovskite antiferromagnets are generated by the G - or C -type antiferromagnetic vectors, instead of the weak ferromagnetic component F [see our $H_{\text{eff}}(\omega_{R,x})$ and $H_{\text{eff}}(\omega_{M,y})$ models]. A magnetic field is able to reorient or switch the G - and C -type magnetic vectors, for example, from G_y to G_z or from G_y to $-G_y$ (see, e.g., Refs. [11,80–82]). Consequently, a magnetic field can manipulate the \mathbf{B}_{eff} field, enabling a pathway towards magnetically controllable ZSSs in perovskite antiferromagnets.

C. The ZSSs with PSTs in antiferromagnetic perovskite semiconductors

To verify our aforementioned analysis, we conduct first-principles simulations focusing on several $Pnma$ perovskite antiferromagnetic semiconductors (see Sec. SII of the SM). Our first choice is CaTcO_3 [83], a G -type antiferromagnet

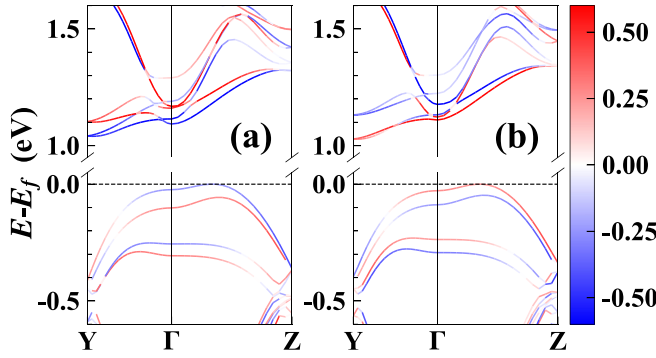


FIG. 2. (a) and (b) Band structures (around the Γ point) of *Pnma* CaTcO₃ with G_y and G_z configurations, respectively. The color bar gives the spin magnetization S_z for the G_y configuration (a) and the spin magnetization S_y for the G_z configuration (b). Here, we set the topmost of the valence bands as E_f . The Brillouin zone is sketched in Fig. S3 of the SM.

with a Néel temperature of ~ 800 K [84]. According to our first-principles calculations, aligning the predominant G -type antiferromagnetic vectors along x , y , and z directions results in relative energies of 0, -0.11 , and -0.36 meV/f.u., respectively. The G_z magnetic configuration thus tends to be more stable than the other two at zero temperature, consistent with experiments [84]. As for the ZSSs in CaTcO₃, we concentrate on the local band structures (e.g., around the Γ point) of the G_y and G_z configurations (see Fig. 2). Strikingly, the topmost valence bands in the vicinity of E_f showcase sizable ZSSs. The ZSSs for the Γ -point energy levels of the G_y and G_z configurations reach ~ 78 and ~ 60 meV, respectively. The spin magnetizations associated with the $(\varepsilon_+, \varepsilon_-)$ sublevels are $(S_{+,z}, S_{-,z}) \approx (-0.251, 0.282)$ for the G_y configuration and $(S_{+,y}, S_{-,y}) \approx (0.271, -0.234)$ for the G_z configuration [85]. The $S_{+,z}$ and $S_{-,y}$ are both negative, but are opposite in sign compared with $S_{-,z}$ and $S_{+,y}$. Besides, the band structures for CaTcO₃ with $-G_y$ and $-G_z$ configurations (see Fig. S4 of the SM) indicate that the spin magnetization is switchable via reversing G_y or G_z antiferromagnetic vectors. These coincide with our aforementioned model analysis regarding $H_{\text{eff}}(\omega_{R,x}) = -\Delta_{R,xyz}\alpha\omega_{R,x}G_y\sigma_z + \Delta_{R,xzy}\alpha\omega_{R,x}G_z\sigma_y$.

To shed light on the role of ω_R and SOC in ZSSs, we compute the band structures for CaTcO₃ with and without the inclusion of SOC and ω_R rotations. As shown in Fig. S5 of the SM, the two topmost valence energy levels showcase ZSSs for G_y and G_z configurations [Figs. S5(a) and S5(d)] [86], while the ZSSs disappear if (i) the SOC is switched off [Figs. S5(c) and S5(f)] or (ii) antiphase ω_R rotations are removed [Figs. S5(b) and S5(e)] [87]. The band structures for other perovskites (e.g., SrTcO₃, YFeO₃, and NaNiF₃) with G -type antiferromagnetic ordering [11, 88–90] present results qualitatively consistent with CaTcO₃ (see Sec. SII of the SM). This confirms the crucial roles of ω_R and SOC in generating ZSSs in *Pnma* perovskites with G -type antiferromagnetism.

Moreover, the spin texture associated with the topmost valence energy levels of CaTcO₃ is nearly homogeneous (i.e., persistent) in momentum space around the Γ point (Fig. 3). As shown in Figs. S9–S11 of the SM, SrTcO₃, YFeO₃, and NaNiF₃ also showcase PSTs. Our first-principles results regarding ZSSs and PSTs in these *Pnma* perovskites validate our analysis in the previous section.

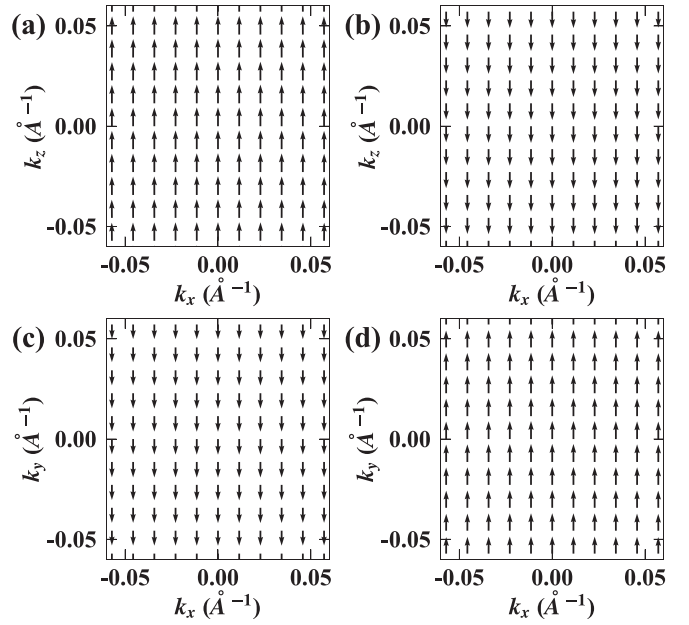


FIG. 3. Spin textures of the *Pnma* CaTcO₃ with G_y [(a) and (b)] and G_z [(c) and (d)] configurations. (a) and (c) [(b) and (d)] are spin textures for the second (first) topmost valence energy levels, around the Γ point. During the calculation, we set $k_y = 0$ and $k_z = 0$ for G_y and G_z configurations, respectively. The lengths of the arrows (at the Γ point) in (a), (b), (c), and (d) represent 0.282, 0.251, 0.234, and 0.271, respectively.

D. The limitation of our models

So far, our models provide descriptions for ZSSs and PSTs in *Pnma* perovskite antiferromagnets; yet they do not correctly capture the values of spin magnetization (see Sec. SIII of the SM). These inconsistencies are ascribed to the limitation of our models. In reality, the spin magnetization is contributed by both electronic spin and orbital degrees of freedom, while our two-level models consider merely spin (the orbital hybridization being fully neglected). Our models thus cannot describe quantitatively the phenomena involving orbital hybridization.

IV. SUMMARY AND OUTLOOK

To summarize, we have found that 12 MPGs can host ZSSs and PSTs. We further identify one mechanism that is responsible for the ZSSs in perovskite antiferromagnets ($Pn'm'a$, $Pnm'a'$, or $Pn'm'a'$ symmetry). Specifically, perovskite antiferromagnets showcase ZSSs thanks to the combination of antiferromagnetic vectors and antiferrodistortive rotations, in the presence of SOC. A magnetic field may manipulate ZSSs in perovskite antiferromagnets by controlling the antiferromagnetic vectors. We also identify CaTcO₃ as an antiferromagnetic semiconductor for the realization of sizable ZSSs and PSTs.

Our work highlights that antiferromagnetic semiconductors can accommodate sizable ZSSs with PSTs. Accordingly, these antiferromagnetic semiconductors are applicable for the design of high-performance spintronic devices. Towards the goal of realizing antiferromagnets of this kind, we propose

the following research avenues: (i) designing $Pn'm'a$, $Pnm'a'$, or $Pn'ma'$ perovskite semiconductors that contain a magnetic B element with a large atomic number Z , as a larger Z implies stronger SOC [91] (i.e., sizable ZSSs), and (ii) exploring sizable ZSSs with PSTs in nonperovskite antiferromagnetic semiconductors [92] following our models shown in Table I.

Note added. Recently, we became aware of a work regarding the spin textures in crystalline materials [93]. Therein, a comprehensive classification of spin textures versus MPGs is provided [93]. Our Table I falls into the category of the Zeeman-type spin textures as shown in Ref. [93]. Furthermore, Ref. [93] indicates that MnTe ($Pnm'a'$ space group, $mm'm'$ point group) showcases ZSSs, which is consistent with our discussion regarding Table I.

ACKNOWLEDGMENTS

We thank the National Key Research and Development Program of China (Grant No. 2022YFA1402502) and the National Natural Science Foundation of China (Grants No. 12274174, No. 52288102, and No. 12034009) for support. L.B. thanks the Department of Defense for support from Vannevar Bush Faculty Fellowship (VBFF) Grant N00014-20-1-2834 and Award No. DMR-1906383 from the National Science Foundation Q-AMASE-i Program (MonArk NSF Quantum Foundry). X.R.L. acknowledges the support from the International Center of Future Science, Jilin University. We also acknowledge the support from the high-performance computing center of Jilin University.

- [1] J. Fabian, A. Matos-Abiague, C. Ertler, P. Stano, and I. Žutić, *Acta Phys. Slovaca* **57**, 565 (2007).
- [2] T. Schäpers, *Semiconductor Spintronics* (De Gruyter, Berlin, 2016).
- [3] L. Tao and E. Y. Tsybal, *J. Phys. D: Appl. Phys.* **54**, 113001 (2021).
- [4] S. Wolf, D. Awschalom, R. Buhrman, J. Daughton, S. von Molnár, M. Roukes, A. Y. Chtchelkanova, and D. Treger, *Science* **294**, 1488 (2001).
- [5] J. D. Koralek, C. P. Weber, J. Orenstein, B. A. Bernevig, S.-C. Zhang, S. Mack, and D. Awschalom, *Nature (London)* **458**, 610 (2009).
- [6] J. Schliemann, J. C. Egues, and D. Loss, *Phys. Rev. Lett.* **90**, 146801 (2003).
- [7] A. Manchon, H. C. Koo, J. Nitta, S. Frolov, and R. Duine, *Nat. Mater.* **14**, 871 (2015).
- [8] Here, $\Delta = 26$ meV corresponds to a temperature of ~ 300 K according to $T = \Delta/k_B$ (k_B being the Boltzmann constant and T being the temperature).
- [9] X. Li and J. Yang, *Natl. Sci. Rev.* **3**, 365 (2016).
- [10] K. Ando, *Science* **312**, 1883 (2006).
- [11] E. Bousquet and A. Cano, *J. Phys.: Condens. Matter* **28**, 123001 (2016).
- [12] T. Jungwirth, J. Sinova, A. Manchon, X. Marti, J. Wunderlich, and C. Felser, *Nat. Phys.* **14**, 200 (2018).
- [13] L.-D. Yuan, Z. Wang, J.-W. Luo, and A. Zunger, *Phys. Rev. Mater.* **5**, 014409 (2021).
- [14] L.-D. Yuan, Z. Wang, J.-W. Luo, and A. Zunger, *Phys. Rev. B* **103**, 224410 (2021).
- [15] L.-D. Yuan, Z. Wang, J.-W. Luo, E. I. Rashba, and A. Zunger, *Phys. Rev. B* **102**, 014422 (2020).
- [16] K. Yamauchi, P. Barone, and S. Picozzi, *Phys. Rev. B* **100**, 245115 (2019).
- [17] S. A. Egorov, D. B. Litvin, and R. A. Evarestov, *J. Phys. Chem. C* **125**, 16147 (2021).
- [18] S. A. Egorov and R. A. Evarestov, *Phys. E (Amsterdam)* **139**, 115118 (2022).
- [19] S. A. Egorov, D. B. Litvin, A. V. Bandura, and R. A. Evarestov, *J. Phys. Chem. C* **126**, 5362 (2022).
- [20] H. Reichlová, R. L. Seeger, R. González-Hernández, I. Kounta, R. Schlitz, D. Kriegner, P. Ritzinger, M. Lammel, M. Leiviskä, V. Petříček, P. Doležal, E. Schmoranzarová, A. Bad'ura, A. Thomas, V. Baltz, L. Michez, J. Sinova, S. T. B. Goennenwein, T. Jungwirth, and L. Šmejkal, *arXiv:2012.15651*.
- [21] R. Ramazashvili, P. Grigoriev, T. Helm, F. Kollmannsberger, M. Kunz, W. Biberacher, E. Kampert, H. Fujiwara, A. Erb, J. Wosnitza, R. Gross, and M. V. Kartsovnik, *npj Quantum Mater.* **6**, 11 (2021).
- [22] R. Ramazashvili, *Phys. Rev. B* **80**, 054405 (2009).
- [23] R. Ramazashvili, *Phys. Rev. Lett.* **105**, 216404 (2010).
- [24] R. Ramazashvili, *Phys. Rev. Lett.* **101**, 137202 (2008).
- [25] R. Ramazashvili, *Phys. Rev. B* **79**, 184432 (2009).
- [26] N. Davier and R. Ramazashvili, *Phys. Rev. B* **107**, 014406 (2023).
- [27] F. Lou, T. Gu, J. Ji, J. Feng, H. Xiang, and A. Stroppa, *npj Comput. Mater.* **6**, 114 (2020).
- [28] H. J. Zhao, X. Liu, Y. Wang, Y. Yang, L. Bellaiche, and Y. Ma, *Phys. Rev. Lett.* **129**, 187602 (2022).
- [29] N. Sivasdas, S. Okamoto, and D. Xiao, *Phys. Rev. Lett.* **117**, 267203 (2016).
- [30] H. Wang and X. Qian, *npj Comput. Mater.* **6**, 199 (2020).
- [31] K. Liu, X. Ma, S. Xu, Y. Li, and M. Zhao, *npj Comput. Mater.* **9**, 16 (2023).
- [32] G. Kresse and J. Furthmüller, *Phys. Rev. B* **54**, 11169 (1996).
- [33] G. Kresse and D. Joubert, *Phys. Rev. B* **59**, 1758 (1999).
- [34] D. M. Ceperley and B. J. Alder, *Phys. Rev. Lett.* **45**, 566 (1980).
- [35] P. E. Blöchl, *Phys. Rev. B* **50**, 17953 (1994).
- [36] See Supplemental Material at <http://link.aps.org/supplemental/10.1103/PhysRevB.108.125108> for structural analysis and several numerical results (band structures and spin textures for various antiferromagnetic semiconductors).
- [37] L. Bellaiche and J. Íñiguez, *Phys. Rev. B* **88**, 014104 (2013).
- [38] P. Chen, M. N. Grisolia, H. J. Zhao, O. E. González-Vázquez, L. Bellaiche, M. Bibes, B.-G. Liu, and J. Íñiguez, *Phys. Rev. B* **97**, 024113 (2018).
- [39] J. E. Auckett, G. J. McIntyre, M. Avdeev, H. De Bruyn, T. T. Tan, S. Li, and C. D. Ling, *J Appl. Crystallogr.* **48**, 273 (2015).
- [40] S. L. Dudarev, G. A. Botton, S. Y. Savrasov, C. J. Humphreys, and A. P. Sutton, *Phys. Rev. B* **57**, 1505 (1998).
- [41] H. Wang, L. He, and X. Wu, *Comput. Mater. Sci.* **96**, 171 (2015).
- [42] H. J. Zhao, L. Bellaiche, X. M. Chen, and J. Íñiguez, *Nat. Commun.* **8**, 14025 (2017).
- [43] The strength of the SOC can be adjusted by changing the “relativistic.F” file in the VASP source code.
- [44] V. Wang, N. Xu, J.-C. Liu, G. Tang, and W.-T. Geng, *Comput. Phys. Commun.* **267**, 108033 (2021).

- [45] VASPkit, <https://vaspkit.com>.
- [46] J. D. Hunter, *Comput. Sci. Eng.* **9**, 90 (2007).
- [47] K. Momma and F. Izumi, *J Appl. Crystallogr.* **44**, 1272 (2011).
- [48] Y. Hinuma, G. Pizzi, Y. Kumagai, F. Oba, and I. Tanaka, *Comput. Mater. Sci.* **128**, 140 (2017).
- [49] A. Togo and I. Tanaka, [arXiv:1808.01590](https://arxiv.org/abs/1808.01590).
- [50] *SEEK-PATH*, <https://www.materialscloud.org/work/tools/seekpath>.
- [51] H. T. Stokes, D. Hatch, and B. Campbell, ISOTROPY Software Suite, <https://stokes.byu.edu/iso/isotropy.php>.
- [52] H. T. Stokes and D. M. Hatch, *J Appl. Crystallogr.* **38**, 237 (2005).
- [53] *FINDSYM*, <https://stokes.byu.edu/iso/findsym.php>.
- [54] See <https://www.wolfram.com/mathematica>.
- [55] M. I. Aroyo, J. M. Perez-Mato, D. Orobengoa, E. Tasci, G. de la Flor, and A. Kirov, *Bulg. Chem. Commun.* **43**, 183 (2011).
- [56] M. I. Aroyo, J. M. Perez-Mato, C. Capillas, E. Kroumova, S. Ivantchev, G. Madariaga, A. Kirov, and H. Wondratschek, *Z. Kristallogr. Cryst. Mater.* **221**, 15 (2006).
- [57] M. I. Aroyo, A. Kirov, C. Capillas, J. M. Perez-Mato, and H. Wondratschek, *Acta Crystallogr. Sect. A: Found. Crystallogr.* **62**, 115 (2006).
- [58] S. V. Gallego, J. M. Perez-Mato, L. Elcoro, E. S. Tasci, R. M. Hanson, K. Momma, M. I. Aroyo, and G. Madariaga, *J. Appl. Crystallogr.* **49**, 1750 (2016).
- [59] S. V. Gallego, J. M. Perez-Mato, L. Elcoro, E. S. Tasci, R. M. Hanson, M. I. Aroyo, and G. Madariaga, *J. Appl. Crystallogr.* **49**, 1941 (2016).
- [60] *MAGNDATA*, <http://webbdcrystal.ehu.es/magndata>.
- [61] *MPOINT*, <https://www.cryst.ehu.es/cryst/mpoint.html>.
- [62] *MTENSOR*, <https://www.cryst.ehu.es/cgi-bin/cryst/programs/mtensor.pl>.
- [63] By this phrase, materials with magnetic moments that are predominantly antiparallel are classified as antiferromagnets, even though there may be some weak ferromagnetic components.
- [64] In antiferromagnets, both ZSSs and weak ferromagnetism can be seen as the result of the effective magnetic field. The weak ferromagnetism is not necessarily the origin of ZSSs.
- [65] Note, however, that the $k_y^2 \mathcal{B}_\alpha \sigma_\beta$ -type coupling is symmetrically allowed once there exists $\Delta_{\alpha,\beta} \mathcal{B}_\alpha \sigma_\beta$.
- [66] H. J. Zhao, H. Nakamura, R. Arras, C. Paillard, P. Chen, J. Gosteau, X. Li, Y. Yang, and L. Bellaiche, *Phys. Rev. Lett.* **125**, 216405 (2020).
- [67] The classification of magnetic space groups can be found at, e.g., <https://www.cryst.ehu.es/cgi-bin/cryst/programs/maggen.gen.pl>.
- [68] L. Bellaiche, Z. Gui, and I. A. Kornev, *J. Phys.: Condens. Matter* **24**, 312201 (2012).
- [69] H. J. Zhao, J. Íñiguez, X. M. Chen, and L. Bellaiche, *Phys. Rev. B* **93**, 014417 (2016).
- [70] M. W. Lufaso and P. M. Woodward, *Acta Crystallogr. Sect. B: Struct. Sci.* **57**, 725 (2001).
- [71] T. Mizokawa, D. I. Khomskii, and G. A. Sawatzky, *Phys. Rev. B* **60**, 7309 (1999).
- [72] Both the *Pnma* and *Pbnm* settings belong to the No. 62 crystallographic space group. In this paper, we employ the standard *Pnma* setting, while references may use the nonstandard *Pbnm* setting. The transformation between *Pnma* and *Pbnm* settings is $(x, y, z)_{Pnma} \rightarrow (y, z, x)_{Pbnm}$ (see p. 5 of Ref. [11]).
- [73] T. Yamaguchi and K. Tsushima, *Phys. Rev. B* **8**, 5187 (1973).
- [74] I. Dzyaloshinskii, *Sov. Phys. JETP* **5**, 1259 (1957).
- [75] I. Dzyaloshinsky, *J. Phys. Chem. Solids* **4**, 241 (1958).
- [76] T. Moriya, *Phys. Rev.* **120**, 91 (1960).
- [77] H. Katsura, N. Nagaosa, and A. V. Balatsky, *Phys. Rev. Lett.* **95**, 057205 (2005).
- [78] D. Rahmedov, D. Wang, J. Íñiguez, and L. Bellaiche, *Phys. Rev. Lett.* **109**, 037207 (2012).
- [79] The spin magnetization carried by quantum state $|\psi\rangle$ is calculated by $S_\alpha = \frac{1}{2} \langle \psi | \sigma_\alpha | \psi \rangle$ (see e.g., Ref. [3]).
- [80] L. A. Prelorendjo, C. E. Johnson, M. F. Thomas, and B. M. Wanklyn, *J. Phys. C: Solid State Phys.* **13**, 2567 (1980).
- [81] J.-H. Lee, Y. K. Jeong, J. H. Park, M.-A. Oak, H. M. Jang, J. Y. Son, and J. F. Scott, *Phys. Rev. Lett.* **107**, 117201 (2011).
- [82] J.-S. Zhou, L. G. Marshall, Z.-Y. Li, X. Li, and J.-M. He, *Phys. Rev. B* **102**, 104420 (2020).
- [83] Note that Tc is an artificial radioactive element with a half-life of $\sim 2 \times 10^5$ yr (see Ref. [84]). Caution should be taken when synthesizing materials containing the element Tc.
- [84] M. Avdeev, G. J. Thorogood, M. L. Carter, B. J. Kennedy, J. Ting, D. J. Singh, and K. S. Wallwork, *J. Am. Chem. Soc.* **133**, 1654 (2011).
- [85] Our aforementioned results are obtained using LSDA+*U*, with $U_{\text{eff}} = 2$ eV added on the *4d* orbitals of Tc (see Sec. II). In general, U_{eff} influences the band structures of materials; these results therefore exhibit some dependencies on U_{eff} . For example, the choice of $U_{\text{eff}} = 1$ eV leads to (i) the Zeeman spin splittings of ~ 82 meV (G_y configuration) and ~ 54 meV (G_z configuration), (ii) $(S_{+,z}, S_{-,z}) \approx (-0.443, 0.452)$ for the G_y configuration, and (iii) $(S_{+,y}, S_{-,y}) \approx (0.462, -0.339)$ for the G_z configuration.
- [86] Note that Figs. S5(a) and S5(d) in the SM are essentially the same as Fig. 2, but with no projection of spin magnetization.
- [87] In *Pnma* ABX_3 perovskites, there are secondary structural distortions, that is, the antipolar displacements of *A* ions denoted by \mathcal{A}_x and \mathcal{G}_z (see Sec. SI of the SM). The \mathcal{A}_x and \mathcal{G}_z distortions come from the combination of ω_R and ω_M rotations of BX_6 octahedrons, via $\mathcal{A}_x \omega_{R,x} \omega_{M,y}$ and $\mathcal{G}_z \omega_{R,x} \omega_{M,y}^2$ couplings [37,38]. From the symmetry point of view, $\mathcal{A}_x \omega_{M,y}$ and $\mathcal{G}_z \omega_{M,y}^2$ act similarly to ω_R (i.e., resembling ω_R). Here, we remove ω_R , \mathcal{A}_x , and \mathcal{G}_z to fully eliminate the influence of ω_R motions on ZSSs.
- [88] E. E. Rodriguez, F. Poineau, A. Llobet, B. J. Kennedy, M. Avdeev, G. J. Thorogood, M. L. Carter, R. Seshadri, D. J. Singh, and A. K. Cheetham, *Phys. Rev. Lett.* **106**, 067201 (2011).
- [89] R. White, *J. Appl. Phys.* **40**, 1061 (1969).
- [90] A. Epstein, J. Makovsky, M. Melamud, and H. Shaked, *Phys. Rev.* **174**, 560 (1968).
- [91] S. L. Dudarev, P. Liu, D. A. Andersson, C. R. Stanek, T. Ozaki, and C. Franchini, *Phys. Rev. Mater.* **3**, 083802 (2019).
- [92] Note that our proposed ZSSs and PSTs are not limited to perovskite antiferromagnets. This is evidenced by our first-principles calculations which demonstrate that *Pcm'n'* $\text{Ca}_2\text{Fe}_2\text{O}_5$ (nonperovskite) presents ZSSs and PSTs for its conduction bands around the Γ point (see Sec. SIV of the SM).
- [93] Y. Liu, J. Li, P. Liu, and Q. Liu, [arXiv:2306.16312](https://arxiv.org/abs/2306.16312).